

PHYSICAL REVIEW D

PARTICLES AND FIELDS

THIRD SERIES, VOLUME 38, NUMBER 2

15 JULY 1988

Noise behavior of the Garching 30-meter prototype gravitational-wave detector

D. Shoemaker,* R. Schilling, L. Schnupp, W. Winkler, K. Maischberger, and A. Rüdiger
Max-Planck-Institut für Quantenoptik, D-8046 Garching bei München, Federal Republic of Germany

(Received 22 February 1988)

The prototype gravitational-wave detector at Garching is described: in a laser-illuminated Michelson interferometer having arms 30 m in length, a folded optical path of 3 km is realized. The origin, action, and magnitude of possible noise sources are given. The agreement between the expected and measured noise is good. For a band of astrophysical interest, extending from 1 to 6 kHz, the quantum shot noise corresponding to a light power of $P = 0.23$ W is dominant. In terms of the dimensionless strain h the best sensitivity in a 1-kHz bandwidth is $h = 3 \times 10^{-18}$, comparable to the most sensitive Weber-bar-type antennas.

I. INTRODUCTION

Various methods have been proposed for the detection of gravitational radiation; two methods have been developed to a point where the chances of a successful search for gravitational-wave events can be realistically assessed. The *resonant bar technique* was pioneered by Weber¹ and followed by further efforts, first with room-temperature bars (Billing *et al.*²) and more recently with cooled bars using very-low-noise superconducting transducers (see Ref. 3 and references therein; also, for the current sensitivities, see Ref. 4). These experiments have put important upper limits on the level of gravitational radiation. The best sensitivities for the gravitational strain h that have been obtained so far are of the order of $h \approx 10^{-18}$.

A different approach is to use *interferometric techniques* to sense changes in the optical path length between widely separated test masses, as first discussed by Gertsenshtein and Pustovoi.⁵ Early workers in this field include Weiss⁶ and Forward.⁷ Since that time a number of groups have pursued this method, and there are now prototype interferometers at MIT,⁸ Glasgow,⁹ Caltech,¹⁰ Orsay,¹¹ and at the Max-Planck-Institut für Quantenoptik, Garching. From the best sensitivity values of these prototypes, as obtained at Garching,¹² and recently also at Glasgow,¹³ one can extrapolate to the sensitivity of large interferometric antennas; an ultimate goal of better than $h \approx 10^{-21}$ seems attainable.

Work on laser interferometers at the Max-Planck-Institute started as early as 1974 (initially at the Institut für Astrophysik, now at the MPI für Quantenoptik) and first concentrated on a 3-m arm-length prototype (Ref. 14 and references therein). After encouraging results it was decided that one could profit from a longer baseline inter-

ferometer (30 m), the construction of which was completed in mid-1983. The goal of the research is to investigate the noise sources in prototype gravitational-wave detectors as an aid in planning full-scale detectors.¹⁵ This paper will describe the 30-m instrument, and particularly its 1986 improvements, in some detail, and it will present the status of the understanding of noise sources observed therein.

The basic design of the 30-m prototype is quite similar to the earlier 3-m prototype;¹⁶ a schematic diagram is shown in Fig. 1. A Michelson interferometer formed of effectively "free" masses is illuminated by an argon-ion laser, with the light path folded in the optical delay-line configuration¹⁷ to increase the sensitivity of the interferometer to gravitational waves. The interference pattern (on diode *D1*) is held to a minimum of intensity by a servosystem, and the control signal of this servo would contain the gravitational-wave signal. This control signal can be interpreted in terms of equivalent mirror displacement x ; this is convenient for comparison with noise sources.

Because the response of the interferometer to gravitationally induced strains is broadband in nature, as are most of the noise sources encountered, it is helpful to work with noise spectral densities (that is, the noise contributed per unit bandwidth). Rigorously, such spectral densities are defined as the *squared* deviations per unit bandwidth, say, in m^2/Hz . It has become customary, however, to express them in *linear* measure, so that the units come out as $\text{m}/\sqrt{\text{Hz}}$. In this paper, such linear spectral densities will be characterized by a tilde above the symbol. In Fig. 2 the spectra of anticipated noise sources are illustrated, expressed as equivalent mirror motion \tilde{x} , calibrated in units of $\text{m}/\sqrt{\text{Hz}}$. To calculate the corresponding sensitivity in gravitational strain,

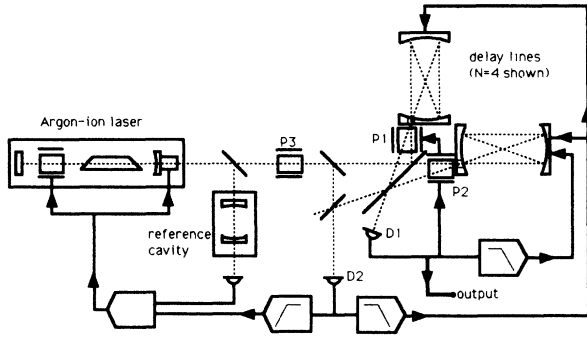


FIG. 1. A schematic view of the interferometer.

$\tilde{h} \equiv \delta l / l$, the mirror motion \tilde{x} is divided by the interferometer arm length l (30 m for the Garching interferometer).

II. QUANTUM NOISE

The two arms of the interferometer are at right angles to each other (Fig. 1). The optical path in each arm is folded in a delay-line configuration and the beams returning from the two delay lines are brought to interference. The separation between the mirrors (which have a radius of curvature of 31.6 m) of the delay line can be varied between 29 and 32 m to obtain the desired number of beams in the delay line. For the data presented here, $N=90$ beams are used, giving a light storage time of $\tau=9 \mu\text{s}$. The separation of the delay-line mirrors can be adjusted with motion-driven translation stages to find the “reentrant condition” for the delay line. This leads to a first-order independence of the path length on tilts, rotations, and lateral translations of the far delay-line mirrors.^{18,19}

The beam splitter and each of the delay-line mirrors are balanced in a simple wire sling pendulum which

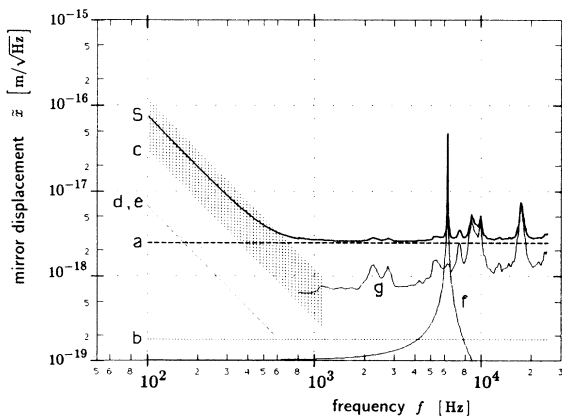


FIG. 2. Spectral densities of various noise sources, expressed as equivalent mirror motion \tilde{x} , in units of $\text{m}/\sqrt{\text{Hz}}$. *a*, photon shot noise; *b*, residual gas fluctuations; *c*, filtered ground motion; *d*, electronic damping system; *e*, pendulum thermal motion; *f*, mirror thermal motion; *g*, laser frequency fluctuations; *S*, quadratic sum of all of the noise sources above.

forms part of the mechanical isolation system (see Secs. IV and V, and Fig. 3), and the other optical components are treated similarly. The coarse alignment of the interferometer is achieved in the vertical axis with rotation of the pendulum suspension points (motor driven) and in the horizontal axis by screw adjustment of the point at which the pendulum wires leave the optical component. Fine adjustment is achieved with offset currents in the coils of the active pendulum damping system (see below); this allows optimization of the contrast in the interferometer. The best contrast $K = (I_{\text{max}} - I_{\text{min}}) / (I_{\text{max}} + I_{\text{min}})$ observed with the 90 beam delay line is $K = 0.992$, I_{max} and I_{min} being the photocurrents at the maximum and the minimum of the interference pattern. The contrast is limited primarily by imperfections in the delay-line mirrors themselves. The optical system holds a contrast of $K \geq 0.96$ for several days without readjustment.

If the only limit to determining the position of the masses were the shot noise of the photocurrent in the photodetector, and if the contrast of the interferometer were perfect, the noise-equivalent position fluctuation would be

$$\tilde{x} = \frac{1}{N} \frac{\lambda}{2\pi} \left(\frac{2e}{I_{\text{max}}} \right)^{1/2} \left(\frac{\pi f \tau}{\sin \pi f \tau} \right), \quad (1)$$

where λ is the wavelength of the light used to illuminate the interferometer, e the elementary charge, and f the measurement frequency. For the storage time τ given, and the frequencies f considered, the factor in the second set of parentheses is close to unity. The finite contrast compromises this sensitivity, as do technical noise sources (Johnson noise in the photodetector, amplifier noise); an expression which takes these factors into account, and which is relevant for the modulation scheme used, is derived in Appendix A. In the ideal case ($K=1.00$, no technical noise), it reduces to the simple form above. For the data presented here (with the experimental conditions $N=90$, $\lambda=514.5 \text{ nm}$, $K=0.96$, $I_{\text{max}}=70 \text{ mA}$, corresponding to a maximum of about 0.23 W on the photodetector), the calculation results in a shot-noise level which is equivalent to a displacement of $2.5 \times 10^{-18} \text{ m}/\sqrt{\text{Hz}}$, shown as curve *a* in Fig. 2. This is a factor 1.25 (2 dB) greater than the ideal case of perfect contrast and no additional noise sources. The influence of radiation pressure fluctuations^{20,6} is completely negligible at the power levels encountered here.

III. FLUCTUATIONS OF RESIDUAL GAS PRESSURE

The entire interferometer is contained in a vacuum system to reduce the effect of refractive index fluctuations and ambient acoustic noise on the apparent path length. The vacuum system has three vertical tanks, 1.0 m in diameter, 1.1 m in height. The “central tank,” which houses the beam splitter, the near delay-line mirrors, and the input optics, is connected to the two “end tanks” (which contain the far delay-line mirrors) by horizontal tubes 0.4 m in diameter. The end tanks are on a system of rails, and it is possible to add extension tubes (maximum length 3 m) to adjust the separation between the

tanks. Only the central tank is in the laboratory; the end tanks are in separate end houses. The horizontal tubes are supported by steel guides on a concrete bed, which in turn is covered by a semicircular concrete cover and about one-half meter of earth. Rotary and turbomolecular pumps allow the system to be pumped from atmospheric pressure (10^5 Pa) to 10^{-2} Pa in 6 h; with the pumps turned off, the system pressure rises to 1 Pa in 24 h. The measurements presented here were performed with pressures between 10^{-1} and 1 Pa.

A noise source to be considered, although not a significant one at present, stems from the residual gas in the vacuum system. The number of molecules in the light path fluctuates, leading to small changes in the apparent optical index, and hence in path length. An estimate²¹ of the magnitude of this effect, valid for the experimental conditions in the 30-m prototype, gives an equivalent mirror motion with a linear spectral density

$$\bar{x} \approx \left[\frac{2\sqrt{3}\pi(n_0-1)^2 \sqrt{l}}{(A_0/V_0)c_0\sqrt{\lambda}} \frac{\sqrt{l}}{N} \left(\frac{p}{p_0} \right) \left[\frac{T_0}{T} \right]^{3/2} \right]^{1/2}, \quad (2)$$

where A_0 is Avogadro's number (6.02×10^{23} molecules/mole), V_0 is the volume of one mole of gas at standard temperature and pressure (22.4×10^{-3} m³/mole), n_0 is the index of refraction of the gas, c_0 is the most probable thermal molecular speed in the gas (for nitrogen at room temperature $T=300$ K, $n_0 \approx 1 + 2.7 \times 10^{-4}$ and $c_0 \approx 400$ m/s), and p_0 and T_0 are the standard pressure and temperature. For these values and typical measurement pressures p one finds $\bar{x} \approx 2 \times 10^{-19}$ m/ $\sqrt{\text{Hz}}$ (curve *b* in Fig. 2).

IV. MOTIONS OF THE OPTICAL COMPONENTS

As mentioned, to isolate the optical components from movement of the suspension point, they are hung as pendulums of length l , and thus of resonant angular frequency $\omega_0 = \sqrt{g/l}$. The $(\omega_0/\omega)^2$ isolation that one would expect from an ideal pendulum is compromised by the finite quality factor Q of the pendulum, and by the suspension wire resonances ("violin string" modes); a model which predicts well the measured transfer function $H(\omega)$ (ratio of mirror motion to suspension point motion) of the suspension system is derived in Appendix B, and the measured and predicted transfer function are plotted in Fig. 6 below. For the pendulums in use at Garching, one finds a transfer function which can be roughly characterized as $(\omega_0/\omega)^2$ to the first "violin string" wire resonance of 212 Hz, then exhibiting a complex resonant structure with an isolation typically better than 10^{-4} .

This wire sling pendulum is suspended in turn from an upper pendulum, consisting of a massive plate suspended by coil springs 0.1 m in length (Fig. 3). In addition to the improvement of the isolation in the longitudinal direction due to the two pendulums in series (see Appendix B), the vertical compliance of the coil spring provides isolation from vertical and rotational motions of the overall support structure which could be cross-coupled into horizontal motion of the optical component. Up to 60 Hz, the measured transfer function (see Fig. 6) of the compound

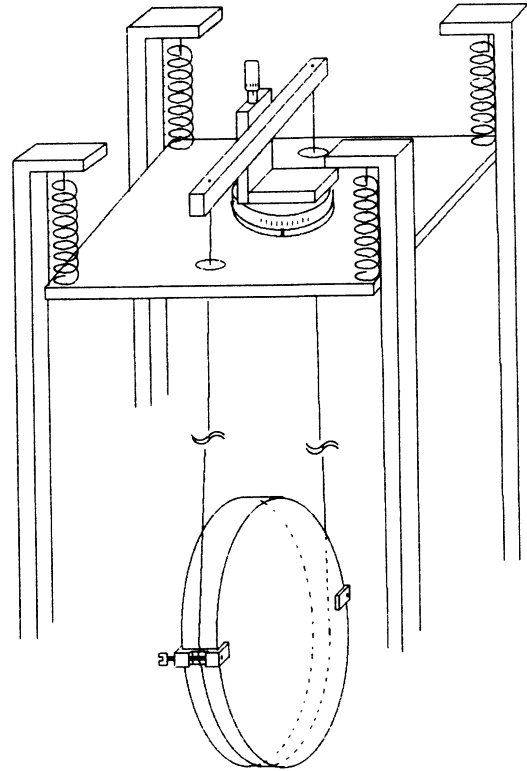


FIG. 3. The seismic isolation system. The upper stage, supported by four coil springs, carries translation and rotation stages for the mirror suspension wire. The upper suspension is 0.10 m in length, the lower 0.72 m. One of the screws for coarse adjustment of mirror tilt is indicated.

(two-stage) pendulum falls as $(\omega_1\omega_0)^2/\omega^4$, where ω_1 and ω_0 are the angular resonant frequencies of the top and bottom pendulums; above a transition section extending from 60 to 200 Hz, the attenuation is typically 10^{-6} . The ground-noise spectrum of the laboratory in Garching, while neither stationary nor smooth, can be roughly characterized by $3 \times 10^{-7} (1 \text{ Hz}/f)^2$ m/ $\sqrt{\text{Hz}}$ between 1 Hz and 1 kHz. Hence, the residual relative motion of the optical components can be estimated, and it is shown as the hatched area labeled as *c* in Fig. 2.

The pendulums are electronically damped at low frequencies²² to prevent large motions due to the ground noise at the resonance frequency. To detect the motion of the pendulum with respect to the suspension point, for each degree of freedom to be damped a small vane is mounted on the optical component, and an infrared light-emitting diode (LED) and opposing silicon photodiode are mounted on the suspension point base. The vane partially interrupts the light, developing a signal proportional to the displacement of the vane. The electronic noise of this transducer, for the geometry used, has a displacement equivalent of 5×10^{-9} m/ $\sqrt{\text{Hz}}$ at 0.75 Hz, and thus is well below the values of the order 10^{-7} m/ $\sqrt{\text{Hz}}$ actually being measured. This electronic noise, from a total of 16 transducers, causes motions of the mirrors via the damping coils (see below). However, the influence of this noise is reduced both electronically by

filters in the damping servoamplifiers and mechanically by the mass of the optical component, leading to expected motions of $10^{-10}(1 \text{ Hz}/f)^4 \text{ m}/\sqrt{\text{Hz}}$, much less than the present sensitivity.

The damping forces are applied by a small permanent magnet mounted integrally with the vane, and an aircore electromagnet mounted concentrically with the LED-photodiode assembly. The coil is positioned so that the magnetic field gradient is maximized at the magnet; this results in the best decoupling of the forces exerted on the optical component from (ground-noise-induced) motion of the coil. Assuming an error in the coil position of as much as 1 mm, and the largest control current possible, the natural ground motion could lead to optical component motions of the order of $4 \times 10^{-14}(1 \text{ Hz}/f)^4 \text{ m}/\sqrt{\text{Hz}}$, a negligible level at the present sensitivity. Noise in the coil current due to the final amplifier, which is left wideband to allow the use of the coil-magnet system in the interferometer locking servosystems, must be taken into account; for the present system, this noise results in a motion of the optical components of $6.8 \times 10^{-14}(1 \text{ Hz}/f)^2 \text{ m}/\sqrt{\text{Hz}}$, illustrated as curve *d* in Fig. 2.

The thermally driven noise of the pendulum can be estimated by considering it as a damped harmonic oscillator; here the Q is that due to the pendulum without electronic damping, because the damping servosystem gain is rolled off at high frequencies. For the thermal motion of an oscillator with an internal energy of $\frac{1}{2}k_B T$ one expects a spectral density

$$\bar{x} = \left(\frac{4k_B T}{mQ\omega_0^3} \right)^{1/2} \left[\frac{1}{\left[1 - \left(\frac{\omega}{\omega_0} \right)^2 \right]^2 + \frac{1}{Q^2} \left(\frac{\omega}{\omega_0} \right)^2} \right]^{1/2} \quad (3)$$

which for the pendulum, in the limit of frequencies high compared with the pendulum resonant frequency, gives $7.4 \times 10^{-14}(1 \text{ Hz}/f)^2 \text{ m}/\sqrt{\text{Hz}}$. This is shown as curve *e* in Fig. 2. Lossy isolation systems (for instance, lead and rubber stacks) have been avoided, as measurements show that only relatively little isolation with a complicated resonance spectrum is achieved. The tendency of such systems to "creep," and their unknown thermally driven motion, make them unattractive for future designs.

The thermally driven motion of the internal modes of the mirrors themselves must also be considered. The delay-line mirrors and the beam splitter are made of circular substrates 150 mm in diameter and 25 mm thick. The previously mentioned wire sling suspension system keeps the mechanical resonances simple and of high Q . The observed frequency of 6.3 kHz for the lowest mode of the mirrors agrees well with calculation²³ for a free cylinder; the Q of this resonance is 500 (limited by the plastic clips which guide the suspension wires, and the material of construction, Zerodur). The motion measured at the peak, $5 \times 10^{-17} \text{ m}/\sqrt{\text{Hz}}$, is about a factor of 7 less than that which one calculates. This can be explained by noting that the lowest mode has radial nodal lines, and the pattern is sampled by the beam spots

roughly equally often on the approaching and receding sections of the mirror, leading to a noticeable cancellation of the effect of the path-length change. The calculated contribution to the displacement noise is shown in curve *f* of Fig. 2. For frequencies much lower than the resonance the noise is at a level of $1 \times 10^{-19} \text{ m}/\sqrt{\text{Hz}}$.

V. FLUCTUATIONS OF LASER LIGHT POWER

The interferometer output falling on diode *D1* (see Fig. 1) is held to a dark fringe with a modulation method.⁶ In both arms of the interferometer, Pockels cells (*P1* and *P2* in Fig. 1) in the light path between the beam splitter and the near-delay-line mirror are used to impress a high-frequency (10-MHz) phase modulation on the light. The light falling on the measurement photodiode *D1* is demodulated, and the resulting error signal is amplified, filtered, and applied to the Pockels cells to hold the intensity on the photodiode to a minimum. The voltage applied to the Pockels cells, which is a linear function of the change of the light path in the delay lines, would carry the gravitational-wave signal. The phase modulation frequency is chosen to be in the frequency range where the amplitude noise of the argon laser is limited (at the power levels used) by the photon shot noise, typically above 5 MHz for the Coherent Innova 90-5 employed. To reduce the light reflected from the measurement photodiode *D1* (EGG type DT110), it is held at the Brewster angle (for silicon $\approx 75^\circ$), thus achieving a quantum efficiency of about 80%.

Keeping the interference pattern at a minimum of intensity reduces the sensitivity of the measurement to amplitude noise in the illuminating laser beam, keeps the intensity on the measurement photodiode *D1* at a manageable level, and allows the other output beam of the interferometer to be used for other purposes. The unity gain frequency in this servoloop must be high for two reasons: first, to give a very large gain at dc, ensuring that the interferometer is held accurately to the dark fringe thus eliminating the influence of low-frequency laser intensity fluctuations on the signal; and second, to give a reliable measurement signal at the highest signal frequency of interest (about 10 kHz). Because, in the present optical arrangement, the light passes through the Pockels cells both before and after the delay line, the unity gain frequency is limited by the time delay in the delay line to about 60 kHz (for 90 beams in the delay line). To reduce the dynamic range of the signal applied to the Pockels cells at very low frequencies (where the signals are largest) this control signal is also sent, suitably filtered, to the damping coils which exert forces on the far mirrors. The unity-gain point in this slow servoloop is set to about 30 Hz, a compromise between dynamic range reduction and the desire not to be acting on the mirrors mechanically in the frequency range of interest (above 100 Hz). This servosystem reduces the influence of amplitude noise to a negligible level.

VI. FLUCTUATIONS OF LASER LIGHT FREQUENCY AND POSITION

The light which illuminates the interferometer must be stabilized in frequency because of imperfections in the

optical system. The delay-line mirrors are not all of exactly the same radius of curvature, which means that meeting the reentrant condition for both delay lines does not result in total path lengths that are exactly equal, but which differ by a static offset ΔL . This directly translates frequency fluctuations $\delta\nu$ into apparent mirror motion \bar{x} (Ref. 16):

$$\bar{x} = \frac{\Delta L}{N} \frac{\delta\nu}{\nu} \quad (4)$$

A total path-length difference of about 2 m is observed when both 90 beam delay lines are reentrant, implying a net mismatch in curvature of about 0.02 m for the present mirrors.

In addition, stray light in the delay lines (due, for instance, to scattering from the mirror surfaces) allows interference between light having traveled different path lengths;^{16,18} for $N=90$ beams in the delay line, the characteristic difference is about 3 km. The high reflectivity of the mirrors allows significant contributions even from "trapped" stray light which has made a large number of round trips of the delay line (corresponding to path differences up to the order of 100 km). The current mirrors employed show a scattering coefficient σ (relative amplitude of the scattered light which then interferes with the main beam) of about 10^{-4} ; given the mirror reflectivity of 0.997, one finds that the fluctuation in apparent path length due to this effect is of the same order of magnitude as that due to the static path-length difference. Thus, the coefficient that relates frequency noise $\delta\nu$ to apparent mirror motion \bar{x} is about 7×10^{-17} m/Hz.

The frequency is stabilized in two steps (see Fig. 1). In the first step,¹⁴ some of the light leaving the laser is directed through a Fabry-Perot reference cavity; the transmitted light intensity is compared with a reference beam intensity, and an error signal is formed. Suitably amplified and filtered, it is applied at low frequencies to a piezoelectric transducer holding one of the laser mirrors, and at high frequencies to an intracavity Pockels cell. The unity-gain frequency of this servoloop is about 400 kHz, limited by the bandwidth of the electronics.

In the second step,¹² a fraction of the light leaving the interferometer on the input side of the beam splitter is brought to interference with a fraction of the input light. The phase difference between these two beams is a function of the average path length in the two arms and the remaining frequency noise on the laser light. The error signal is developed with a modulation-demodulation scheme similar to that described for the main signal path, utilizing Pockels cell *P3* and photodiode *D2*. At frequencies in the range of a few hertz, the Fabry-Perot cavity is the more stable reference, and the error signal is used to prevent common-mode motion of the delay-line mirrors (i.e., the interference pattern on *D2* is held to a minimum of intensity). At frequencies higher than a few tens of hertz, the length of the delay line is a quiet and more sensitive length reference; the error signal in this frequency range is fed back to the laser. The gain possible in this servoloop is primarily limited by the time delay in the delay line; for a storage time of 9 μ s (corresponding to

$N=90$ beams in the delay line) it is about 60 kHz. An estimate of the influence on the interferometer of the remaining frequency noise is shown as curve *g* in Fig. 2. The resonance structures seen around 10 kHz are due to thermally driven motions in the Fabry-Perot cavity.

Fluctuations in the beam geometry can be translated into apparent mirror motions.²² In a simple Michelson interferometer, a misalignment of the beam splitter leads to a sensitivity to changes in the beam position; a difference in the length of the two arms leads to a sensitivity to beam direction. In addition, there remains a sensitivity due to irregularities in the optical components (mirrors and Pockels cells in particular) even when the interferometer is well aligned and symmetrized.

A single-mode optical fiber is used to suppress such fluctuations in the beam geometry²⁴ and to carry the light from the laser table into the vacuum. The fiber employed here (the fiber used is an experimental type, unfortunately not in production, kindly donated by AEG) has a mode radius $w = 2.7 \mu\text{m}$, and microscope objectives (10 \times) are used to couple into and out of the fiber. It is not a polarization-holding fiber, and to correct for slow thermal drifts in the polarization a $\lambda/2$ plate in front of the input to the fiber is used. The fiber output assembly is isolated from ground noise by suspending it on an electronically damped pendulum mass; this is necessary to obtain a jitter-free beam, and allows convenient adjustment of the input beam angle and position as well.

A coefficient for the sensitivity to beam motion can be obtained by giving a calibrated motion to the beam and viewing the effect in the apparent mirror motion spectrum, which in the system with $N=90$ bounces gave 2×10^{-6} m/rad. Attempts to measure the residual beam jitter after the fiber are limited by measurement noise (shot noise in the quadrant photodiode current) at 3×10^{-12} rad/ $\sqrt{\text{Hz}}$ for all frequencies higher than 50 Hz. Thus the *upper limit* for the influence of beam jitter on the interferometer spectrum lies at 6×10^{-18} m/ $\sqrt{\text{Hz}}$, a factor of 2 higher than the observed interferometer noise level in the kilohertz range; clearly, a more sensitive independent measurement of the beam motion after the fiber is needed before it can be eliminated as a possible noise source.

VII. PERFORMANCE OF THE INTERFEROMETER

Estimates of the contribution to the noise "budget" by each of the noise sources mentioned above have been made in Fig. 2, as well as a quadratic sum of all of these sources (curve *S*). The figure for beam jitter is not included in this sum because it is only an upper limit. The output signal of the interferometer—the control signal for the Pockels cells in the arms of the interferometer—is usually analyzed by a Fourier-transform spectrum analyzer (hp3582A). Continuous measurements of 30 min or an hour are possible, and when the interferometer loses "lock" (usually due to a longitudinal mode hop in the laser) the servosystems are automatically sequentially "relocked." Figure 4, curve *A*, is a composition of several 2-min averages at different sampling rates (to cover the broad frequency range presented), resulting in the relatively small uncertainty in the noise level. Also

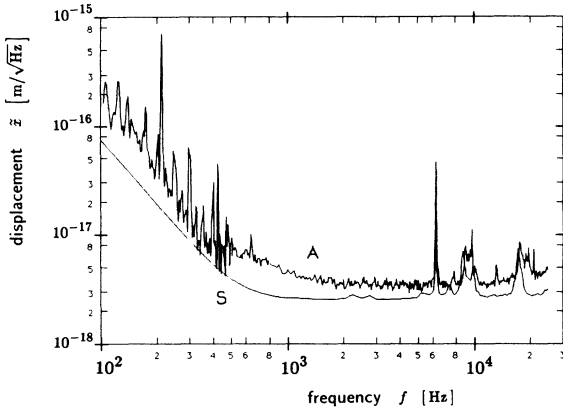


FIG. 4. The interferometer noise spectrum. *A*, measured; *S*, predicted.

shown is the quadratic sum of all noise sources (curve *S*); it is seen that the noise is in excess of the estimate.

Up to frequencies of several hundred hertz, multiples of the 50-Hz main supply are quite evident. Also seen are several suspension wire resonances (at 212 and 424 Hz). The overall level lies above that predicted; possible explanations are that remaining cross coupling in the pendulum isolation system allows ground motion to drive the mirrors, or that there is insufficient decoupling between the laser and the interferometer.

At higher frequencies the mirror resonances at 6.3 kHz are visible, as is the remaining influence of resonances in the Fabry-Perot cavity used as the frequency stabilization reference. There are still contributions from the mains harmonics, although they are not resolved in the spectrum. In the quietest frequency band, between 1 and 6 kHz, there is a discrepancy of a factor of 1.4 (or in logarithmic measure 3 dB) between the predicted shot-noise level and that observed. Experiments with the 0.3-m interferometer (see Appendix C), and with different power levels (see Appendix A), suggest that this excess consists of two parts: a discrepancy between the calculated and observed shot noise, which causes a scaling error (i.e., a constant error in logarithmic measure) of 1.06; and a constant noise (measured in mirror displacement) at a level of 2.5×10^{-18} m/ $\sqrt{\text{Hz}}$. The latter noise source could be one (or several) of the previously mentioned white-noise sources. To gain more knowledge in this frequency regime the shot-noise limit must be significantly reduced, requiring considerably more light power.

VIII. CONCLUSION

The Garching prototype interferometer, with an optical path of 90×30 m, is very close to the shot-noise limit calculated for the relatively high power available, and over a broad frequency range of astrophysical interest. Even though this *prototype* has a delay-line storage time of only 9 μs , it already has a sensitivity (expressed as an equivalent dimensionless strain h of 3×10^{-18} in a 1-kHz bandwidth) which for many predicted sources is comparable to the most sensitive bar-type antennas.²⁵ Optimizing the storage time for the frequency range envisaged

would allow an increase in sensitivity by almost 2 orders of magnitude. Much of the technology developed here can be extended to full-scale gravitational-wave interferometers,¹⁵ leading to optimism for the feasibility of gravitational-wave detection in the near future.

APPENDIX A: CALCULATION OF THE SHOT NOISE

The current $I_{\text{ph}}(t)$ in the measurement photodiode *D* 1 is

$$I_{\text{ph}}(t) = I_{\text{min}} + \frac{I_{\text{max}} - I_{\text{min}}}{2} [1 - \cos\phi(t)] \quad (\text{A1})$$

with

$$\phi(t) = kx + \phi_m \sin\omega_m t \quad (\text{A2})$$

and

$$x = x_0 + \delta x(t), \quad (\text{A3})$$

where $k = (2\pi)/\lambda$, x_0 the static difference in optical path between the arms of the interferometer (the “operating point”), $\delta x(t)$ the signal (small in comparison with λ , and slowly changing in comparison with the modulation frequency), ϕ_m the amplitude of the high-frequency phase modulation applied by the Pockels cells, and ω_m the modulation frequency. This photodiode current can be expanded in a series of Bessel functions $J_n(\phi_m)$; keeping only the lowest-order terms (this corresponds to bandpass filtering the photodiode signal around the modulation frequency and at dc) one finds

$$I_{\text{dc}} = I_{\text{min}} + \frac{I_{\text{eff}}}{2} [1 - J_0(\phi_m) \cos kx] \quad (\text{A4})$$

and

$$I_{\omega_m} = \frac{I_{\text{eff}}}{2} 2J_1(\phi_m) \sin kx \sin\omega_m t, \quad (\text{A5})$$

with an effective current swing of $I_{\text{eff}} = (I_{\text{max}} - I_{\text{min}})$.

The servosystem is arranged to hold the output of the interferometer on diode *D* 1 at a minimum of intensity; this corresponds to $kx \ll 1$ (modulo 2π), or

$$I_{\text{dc}} \approx I_{\text{min}} + \frac{I_{\text{eff}}}{2} [1 - J_0(\phi_m)] \quad (\text{A6})$$

and

$$I_{\omega_m} \approx I_{\text{eff}} J_1(\phi_m) k \delta x(t) \sin\omega_m t. \quad (\text{A7})$$

The signal is demodulated by multiplying by a square wave at ω_m ; taking a net mixer gain of R , and keeping only terms around dc, one finds

$$V_{\text{sig}} = RI_{\text{eff}} J_1(\phi_m) k \delta x(t). \quad (\text{A8})$$

The noise that competes with this signal is the shot noise due to the flow of current in the photodiode I_{dc} , and the technical noise sources (Johnson noise of the photodiode internal resistance, amplifier electronic noise). The latter can be characterized as an additional fixed virtual current I_{det} in the photodiode. The noise due to these two currents is white and has a linear spectral den-

sity of $\sqrt{2e(I_{dc} + I_{det})}$ at the photodiode; it is filtered by the photodiode amplifier so that the amplitude is negligible for frequencies outside of the band $\omega_m \pm \omega_{sig}$, with ω_{sig} the (angular) signal frequency. This noise is then multiplied by the square wave in the mixer, resulting in noise components which are mixed down to the signal frequency:

$$\bar{V}_{noise} = R\sqrt{2}\sqrt{2e(I_{dc} + I_{det})}. \quad (A9)$$

The $\sqrt{2}$ is due to the fact that the noise above and below the carrier are mixed down to the same low (positive) frequency, and add incoherently.

Equating the signal and the noise, one finds that the equivalent displacement noise due to the shot noise can be expressed by the linear spectral density

$$\bar{x}_{shot} = \frac{1}{k}\sqrt{2}\frac{\sqrt{2e(I_{dc} + I_{det})}}{J_1(\phi_m)I_{eff}}. \quad (A10)$$

The expression for \bar{x}_{shot} as a function of ϕ_m has a gentle minimum, and the ϕ_m corresponding to this minimum should be applied to observe the highest sensitivity. The signal which is used for the output of the interferometer is the control signal to the Pockels cells; in the limit of large loop gain, this voltage is related to the position noise via the Pockels cell voltage V_λ that causes a change in optical path by one wavelength λ . Then the noise voltage expected for the shot-noise limit is

$$\bar{V}_{shot} = \frac{V_\lambda \bar{x}_{shot}}{\lambda}. \quad (A11)$$

An approximate expression, valid for typical contrasts ($K > 0.9$) and modulation depths ($I_{dc} < 0.2I_{max}$), simplifies the calculation of the voltage shot noise \bar{V}_{shot} :

$$\bar{V}_{shot} \approx \frac{V_\lambda}{2\pi} \left[\frac{2e(I_{dc} + I_{det})}{(I_{dc} - I_{min})I_{eff} - \frac{3}{2}(I_{dc} - I_{min})^2} \right]^{1/2}. \quad (A12)$$

Under these circumstances, an approximation giving the optimum modulation depth can be found. The observable quantity $I_{dc,opt}$ corresponding to this optimum is

$$I_{dc,opt} \approx \left[\frac{2}{3}(I_{min} + I_{det})I_{max} \right]^{1/2}. \quad (A13)$$

Measurements were performed on the 30-m and simplified 0.3-m interferometers (Appendix C) to verify the accuracy of the exact expressions. The photodiode currents I_{max} , I_{min} , and I_{dc} were monitored with a precision resistor; the technical noise was measured by comparison with the noise due to an incandescent lamp at frequencies near the modulation frequency of 10 MHz where it is assumed that the lamp has no noise above shot noise. The V_λ for the Pockels cells was measured *in situ* by finding the voltage step which resulted in a change of exactly one λ of optical path length in the cell, and tested separately for nonlinearity (the voltage for a jump of 2λ is within high precision twice that needed for 1λ).

With the $N = 90$ beam interferometer operating under

normal conditions, the voltage noise on the Pockels cells in the quietest frequency range (4–5 kHz) was observed for a variety of conditions (changes in illuminating intensity, depth of modulation, contrast, and excess white light on the photodetector). A fit was made to the experimental data with three free parameters: scale factors β and κ which describe errors in V_λ and I_{det} , respectively, and an additive constant ϵ which describes a constant excess noise motion of the mirrors:

$$\bar{V}_{shot,fit}^2 = \left[\frac{\beta V_\lambda}{2\pi} \right]^2 \frac{4e(\kappa I_{det} + I_{dc})}{J_1^2(\phi_m)I_{eff}^2} + \epsilon^2. \quad (A14)$$

The argument ϕ_m in the Bessel function $J_1(\phi_m)$ can be derived from the measured values I_{dc}, I_{min}, I_{eff} , as shown in the beginning of this appendix.

The result for the 30-m interferometer is shown in Fig. 5, where the *measured* noise in V^2/Hz is the independent variable and the *calculated* noise in V^2/Hz is the dependent variable, and the measured points are compared with the ideal case, a one-to-one relationship. A logarithmic graph was chosen to allow the large range of values to be clearly presented; however, a graph *linear* in both axes is a more useful diagnostic tool, with the advantage of allowing errors in the fit to appear in a simple graphical form. For instance, an error in the Pockels cell coefficient V_λ appears as a slope error, a constant additive noise ϵ as a displacement, and an error in the effective technical noise current I_{det} as a deviation from that which should be a straight line. For the data presented, the best β is 1.06, the best κ is 0.88, and the best ϵ is $2.37 \times 10^{-7} V/\sqrt{Hz}$ (the latter corresponding to a noise in mirror displacement of $2.5 \times 10^{-18} m/\sqrt{Hz}$). Because the origin of these differences from the expected values is not yet explained, the equation without modification is used to calculate the expected shot-noise limit for the 90 beam delay-line interferometer, as given

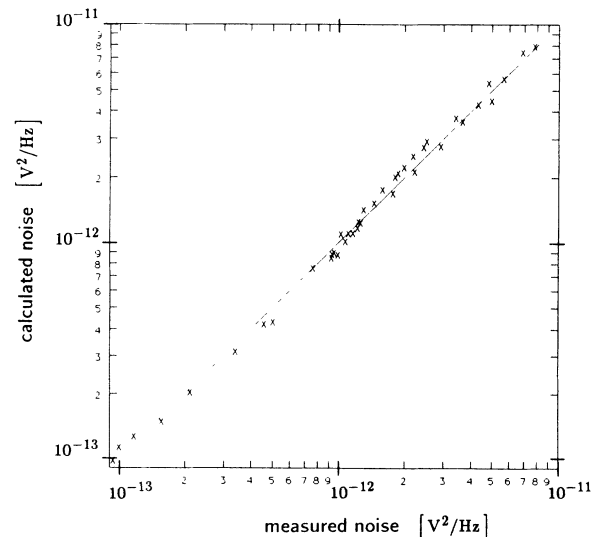


FIG. 5. Comparison of measured and calculated shot noise. The solid line indicates the locus of perfect agreement between measured and calculated noise levels.

in Fig. 2. However, it is reassuring that the errors are small, and that the functional dependence of the noise is correct.

APPENDIX B: TRANSFER FUNCTION OF THE PENDULUM ISOLATION SYSTEM

The pendulum can be treated in close analogy to an electrical (loss-free) transmission line, terminated with an inductance (to represent the inertial termination by the impedance $Z_p = i\omega m$ of the pendulum mass m). The characteristic impedance $Z = \sqrt{mg\gamma}$ of the mechanical transmission line is given by the tensile force mg on the wire and the linear mass density γ . The propagation constant $k = \omega/v_{tr}$ is determined by the velocity $v_{tr} = \sqrt{mg/\gamma}$ with which a transverse motion propagates along the wire.

As in an electrical transmission line, the displacement x_p at the termination (pendulum mass) is transformed to the front end (suspension point) via a transformation

$$x_0 = x_p \left[\frac{Z_p}{Z} i \sin kl + \cos kl \right], \quad (\text{B1})$$

and one arrives at the transfer function magnitude

$$H(\omega) \equiv \frac{x_p}{x_0} = \frac{1}{\cos kl - \frac{\omega m}{Z} \sin kl}. \quad (\text{B2})$$

The lowest resonance $\omega_p = \sqrt{g/l}$ (the pendulation mode) and the well-known low-frequency transfer function $H(\omega) = [1 - (\omega/\omega_p)^2]^{-1}$ are easily derived by expanding for $kl \ll 1$; for $l = 0.72$ m we have $f_p = \omega_p/2\pi \approx 0.59$ Hz.

All further resonances (the ‘‘violin string’’ resonances at ω_n) can be found from the approximation $kl \approx n\pi$, leading to

$$\omega_n \approx n\pi\omega_p \left(\frac{m}{\mu} \right)^{1/2}, \quad (\text{B3})$$

with $\mu = \gamma l$ the mass of the wire sling (two wires). In between these resonances, the transfer function $H(\omega)$ provides an isolation that is at best

$$H(\omega) \approx \frac{Z}{\omega m} = \frac{\omega_p}{\omega} \left(\frac{\mu}{m} \right)^{1/2}. \quad (\text{B4})$$

For the values used ($m = 1.1$ kg, steel wire 0.1 mm in diameter), the mass ratio m/μ is about 12 500, and the wire resonances are in very good agreement with the measured peaks at multiples of $f_1 \approx 212$ Hz. At these frequencies, the pendulum suspension not only loses its isolation feature, it may even enhance the pendulum mass motion. Figure 6 shows the measured (curve *a*) and calculated (curve *b*) transfer functions. The additional peaks observed in the measured transfer function at 300 and 550 Hz are due to pickup of harmonics of the 50-Hz line frequency.

The influence of the damping due to internal losses in the suspension system can be thought of as entering in two ways: first, as a modification in the high-frequency

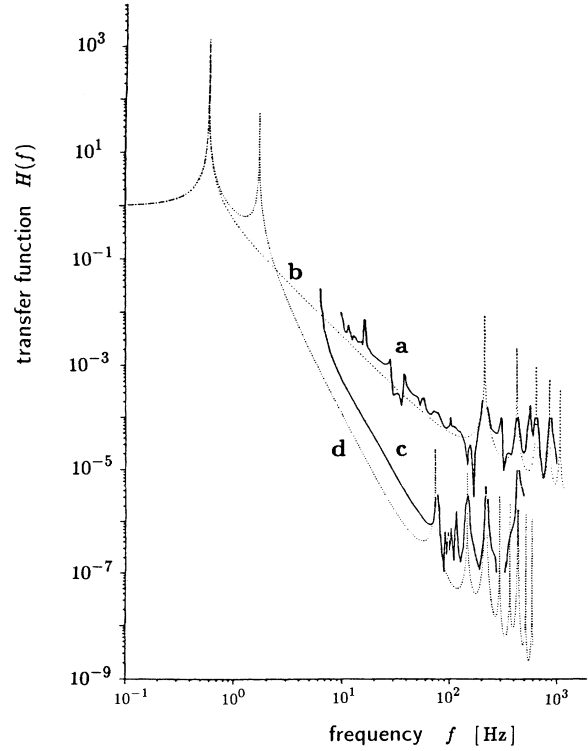


FIG. 6. Pendulum transfer functions. *a*, measured, single stage; *b*, calculated, single stage; *c*, measured, double stage; *d*, calculated, double stage.

transfer function of the simple pendulum model, and second, as a change in the form of the ‘‘violin string’’ resonances. The finite Q of the pendulum motion, in particular if it is due to internal friction in the suspending wires, causes a transition from $H \approx (\omega_0/\omega)^2$ to $H \approx \omega_0/(\omega Q)$ at a transition frequency of $(\omega_0/2\pi)Q$. However, under normal conditions, the pendulum Q is primarily limited by damping from the residual gas: the measured pendulum Q shows a monotonic dependence on the residual gas pressure. At the lowest pressure attainable (10^{-3} Pa) it reaches $Q_{\max} = 10^5$; at the normal operating pressure of 1 Pa, it is $Q = 3 \times 10^4$. If we take this Q_{\max} as an upper limit for the internal losses, one calculates a transition frequency f_Q on the order of 10^5 Hz where the transfer function is dominated by the string resonances. These string resonances have measured Q 's of the order of 2×10^4 , which does not lead to a significant compromise of the transfer function; the primary effect is to keep the wire resonant peaks in the transfer function finite, in our case at values below unity. Thus, damping mechanisms do not significantly influence the performance of the isolation system.

The two-stage pendulum currently in use at Garching can be similarly analyzed. By twofold application of the transformation from the pendulum mass to the driving point, a transfer function for the compound pendulum is found. In contrast with the single pendulum, where there are no free parameters, it is necessary to characterize the coil springs (which form the upper pendulums) in terms of a linear mass density based on the measured transverse

resonant frequencies and the length of the springs. With this parameter adjusted for the best fit, the measured and calculated transfer functions (in Fig. 6, curves *c* and *d*, respectively) again are in reasonably good agreement.

The measurement of the pendulum transfer function is made difficult by the large (120 dB) difference in amplitudes of mechanical motion between the pendulum suspension point and the mirror, and all acoustical or mechanical “short circuits” must be carefully avoided. For this reason, the measurement is performed entirely in the vacuum system of the interferometer. The pendulum suspension point of one of the far delay-line mirrors is driven parallel to the interferometer arm axis by an electromagnetic “shaker.” The motion at this point is monitored with a piezoelectric accelerometer (Endevco model 7705-1000), and the motion of the mirror is measured with the aid of the $N=90$ beam interferometer. The driving function for the “shaker” is a swept sine wave, the frequencies close to the “violin string” resonances having been avoided. A two-channel Fourier transform spectrum analyzer (hp3582A) calculates the raw transfer function, which is then corrected for the accelerometer response and the interferometer low-frequency servoloop. The resulting measured transfer functions agree well with the predictions (see Fig. 6).

APPENDIX C: THE 0.3-m INTERFEROMETER

An alternative configuration of the interferometer is formed by turning the near delay-line mirrors around so that the beam is immediately returned to the beam splitter, for a total path of 0.6 m. The sensitivity of the interferometer to mirror motion is much reduced, and the optical path is simplified. The reduction of scattered light and the ability to bring the interferometer to near perfect symmetry strongly reduces the constraints on the laser frequency stabilization. The frequency stabilization servoloop bandwidth achievable with the piezo-controlled laser mirror suffices, and this allows the operation of the laser without its internal Pockels cell, leading

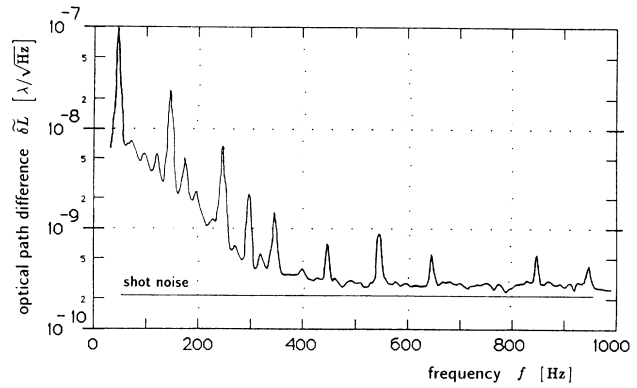


FIG. 7. Noise spectrum of the 30-cm test interferometer. The horizontal line represents the calculated shot noise for the experimental conditions. The regularly spaced peaks are caused by electrical disturbances from harmonics of the 50-Hz line frequency.

to higher output powers and thus more light in the interferometer.

However, the interferometer fringe detection electronics are the same as for the 30-m interferometer, and the Pockels cells are still used in the same manner; this allows tests of much of the system without the added complications associated with the delay lines. In particular it has proven invaluable for helping to locate mechanical resonances. Except for the expected contributions of ground noise (below several hundred hertz) and thermally driven resonances of the optical components (above 6 kHz), the noise spectrum is limited by the shot noise in the measurement. A sample spectrum is shown in Fig. 7, for which $I_{\max}=233$ mA, and $I_{\min}=0.7$ mA; this corresponds to a contrast $K=0.994$. In addition to indicating that the measurement system works properly at this level, $\delta L = 2.4 \times 10^{-10} \lambda / \sqrt{\text{Hz}}$, it is reassuring to see that the optical fiber and the Pockels cells do not display anomalous effects with light powers on the order of 1 W.

*Present address: CNRS, Bâtiment 104, 91405 Orsay, France.

¹J. Weber, Phys. Rev. Lett. **22**, 1320 (1969).

²H. Billing, P. Kafka, K. Maischberger, F. Meyer, and W. Winkler, Lett. Nuovo Cimento **12**, 111 (1975).

³V. B. Braginsky and K. S. Thorne, in *Present Status of Gravitational-Wave Experiments*, proceedings of the Ninth International Conference on General Relativity, Jena, Germany, 1980, edited by E. Schmutzer (Cambridge University Press, Cambridge, England, 1983), pp. 239–253.

⁴*Proceedings of the Fourth Marcel Grossmann Meeting on General Relativity*, Rome, 1985, edited by R. Ruffini (Elsevier, New York, 1986).

⁵M. E. Gertsenshtein and V. I. Pustovoit, Zh. Eksp. Teor. Fiz. **43**, 605 (1962) [Sov. Phys. JETP **16**, 433 (1963)].

⁶R. Weiss, MIT Research Laboratory of Electronics Report No. 105, 1972 (unpublished).

⁷R. L. Forward, Phys. Rev. D **17**, 379 (1978).

⁸J. Livas, R. Benford, D. Dewey, A. Jeffries, P. Saulson, D. Shoemaker, and R. Weiss, in *Proceedings of the Fourth Marcel*

Grossmann Meeting on General Relativity (Ref. 4), pp. 591–597.

⁹G. P. Newton, J. Hough, G. A. Kerr, B. J. Meers, N. A. Robertson, H. Ward, J. B. Mangan, and S. Hoggan, in *Proceedings of the Fourth Marcel Grossmann Meeting on General Relativity* (Ref. 4), pp. 599–604.

¹⁰R. Spero, in *Proceedings of the Fourth Marcel Grossmann Meeting on General Relativity* (Ref. 4), pp. 615–620.

¹¹A. Brillat (private communication).

¹²D. H. Shoemaker, W. Winkler, K. Maischberger, A. Rüdiger, R. Schilling, and L. Schnupp, in *Proceedings of the Fourth Marcel Grossmann Meeting on General Relativity* (Ref. 4), pp. 605–614.

¹³H. Ward *et al.*, in *The Glasgow Gravitational Wave Detector—Present Progress and Future Plans*, proceedings of the International Symposium on Experimental Gravitational Physics, Guangzhou, People’s Republic of China, 1987 (World Scientific, Singapore, in press).

- berger, and L. Schnupp, in *Quantum Optics, Experimental Gravitation, and Measurement Theory*, edited by P. Meystre and M. O. Scully (Plenum, New York, 1983), pp. 525–566.
- ¹⁵W. Winkler, K. Maischberger, A. Rüdiger, R. Schilling, L. Schnupp, and D. H. Shoemaker, in *Proceedings of the Fourth Marcel Grossmann Meeting on General Relativity* (Ref. 4), pp. 621–630.
- ¹⁶H. Billing, K. Maischberger, A. Rüdiger, R. Schilling, L. Schnupp, and W. Winkler, *J. Phys. E* **12**, 1043 (1979).
- ¹⁷D. Herriot, H. Kogelnik, and R. Kompfner, *Appl. Opt.* **3**, 523 (1964).
- ¹⁸W. Winkler, Ph.D. thesis, München Internal Report No. MPQ 74, 1983 (unpublished).
- ¹⁹P. Linsay, P. Saulson, and R. Weiss, *A Study of a Long Baseline Gravitational Wave Antenna System* (MIT, Cambridge, MA, 1983).
- ²⁰W. Winkler, in *A Laser Interferometer to Search for Gravitational Radiation*, proceedings of the International Meeting on Experimental Gravitation, Pavia, 1976 (Accademia Nazionale dei Lincei, Rome, 1977), pp. 351–363.
- ²¹A. Rüdiger (unpublished).
- ²²K. Maischberger, A. Rüdiger, R. Schilling, L. Schnupp, W. Winkler, and H. Billing, in *Proceedings of the Second Marcel Grossmann Meeting on General Relativity*, Trieste, 1979, edited by R. Ruffini (North-Holland, Amsterdam, 1982), pp. 1083–1100.
- ²³J. R. Hutchinson, *ASME J. Appl. Mech.* **47**, 901 (1980).
- ²⁴R. Weiss (private communication).
- ²⁵D. Dewey, *Phys. Rev. D* **36**, 1577 (1987).